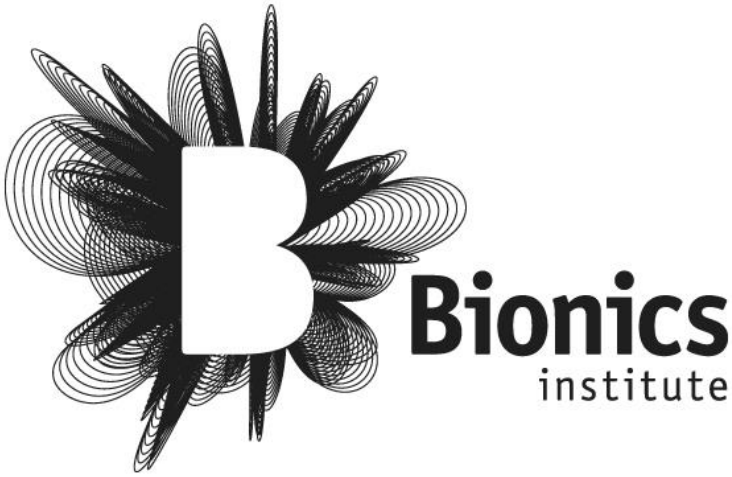

An all-diamond, hermetic electrical feedthrough array for a retinal prosthesis

Kumaravelu Ganesan[a], David J. Garrett[a,*], Arman Ahnood[a], Mohit N. Shivdasani[b], Wei Tong[a], Ann M. Turnley[c], Kate Fox[a], , Hamish Meffin[d,e], Steven Prawer[a]

[a] *School of Physics, The University of Melbourne, Victoria 3010, Australia*

[b] *The Bionics Institute, 384-388 Albert Street, East Melbourne, Victoria 3002, Australia*

[c]*The Centre for Neuroscience, Department of Anatomy and Neuroscience University of Melbourne, Victoria 3010, Australia*

[d] *NICTA, Department of Electrical and Electronic Engineering, University of Melbourne, Victoria 3010, Australia*

[e] *Department of Electrical and Electronic Engineering, The University of Melbourne, Victoria 3010, Australia*

** Corresponding Author:* David J. Garrett, Email: dgarrett@unimelb.edu.au, Ph: +61 3 9035 4973

Abstract

The interface between medical implants and the human nervous system is rapidly becoming more and more complex. This rise in complexity is driving the need for increasing numbers of densely packed electrical feedthroughs to carry signals to and from implanted devices. This is particularly crucial in the field of neural prosthesis where high resolution stimulating or recording arrays near peripheral nerves or in the brain could dramatically improve the performance of these devices. Here we describe a flexible strategy for implementing high density, high count arrays of hermetic electrical feedthroughs by forming conducting nitrogen doped nanocrystalline diamond channels within an insulating polycrystalline diamond substrate. A unique feature of these arrays is that the feedthroughs can themselves be used as stimulating electrodes for neural tissue. Our particular application is such a feedthrough, designed as a component of a retinal implant to restore vision to the blind. The hermeticity of the feedthroughs means that the array can also form part of an implantable capsule which can interface directly with internal electronic chips. The hermeticity of the array is demonstrated by helium leak tests and electrical and electrochemical characterisation of the feedthroughs is described. The nitrogen doped nanocrystalline diamond forming the electrical feedthroughs is shown to be non cyctotoxic. New fabrication strategies, such as the one described here, combined with the exceptional biostability of diamond can be exploited to generate a range of biomedical implants that last for the lifetime of the user without fear of degradation.

1. Introduction

Implantable electronic devices must necessarily adhere to a very strict set of standards before they can be approved for clinical use. One of these standards is the requirement that electronically active components such as microprocessors must be encapsulated in a hermetically encapsulated [1], to protect the body from the toxicity of conventional electronic components and as well as to to protect the components from the harsh environment inside the body which leads to accelerated device failure. Encapsulation materials such as titanium or ceramics have a long history of success in devices such as pace-makers and cochlear implants [1]. Such materials are impermeable to water or gasses and are very well tolerated by the body. The critical complication in most implantable devices is the need to cross the wall of the encapsulation with electrically conducting wires, commonly called a feedthrough. Very often wires are required to supply power and data to components sealed with in the hermetic capsule. In some cases, wires may also be required to carry electrical impulses to or from neural populations targeted by the device. Feedthroughs are understandably one of the most common failure points of hermetic capsules and therefore must be a carefully considered element in the design of any implantable device.

The feedthrough array discussed in this paper is designed to perform both as an electronics encapsulation and as a stimulation interface to the retinal tissue for an epi-retinal vision prosthesis. Recently there have been significant advances in the field of bionic vision [2-6] including the world's first commercially available implant [7]. Retinal prostheses consist of an array of stimulating electrodes that are surgically implanted against the surface of the retina. They are typically positioned on or close to the macular region of the retina, the area responsible for high acuity vision [8]. The devices are designed to treat diseases such as retinitis pigmentosa where the light detection cells within the retina are damaged but most of the inner middle retinal neurons such as ganglion and bipolar cells survive. These surviving cells can be electrically stimulated with an array of electrodes resulting in recipients perceiving an array of spots (or phosphenes) which can be used to form a crude image. Current state of the art epi-retinal devices tend to have around 60 electrodes positioned close to the retina providing the user with low resolution vision. An obvious potential precursor to achieving a higher resolution outcome for the patient is to employ higher numbers of electrodes positioned closer together. High numbers of stimulating electrodes require a large numbers of feedthroughs from the control electronics with the result that the reliability of an

individual feedthrough must be extremely good. Very often arrays of stimulating electrodes are connected to the electronics capsule by a flexible leadwire. When hundreds or thousands of electrodes are called for, individual wiring of each electrode and routing wires to remote capsule becomes untenable, in particular in the eye where physical space is limited.

Figure 1 shows an illustration of the approach currently employed by Bionic Vision Australia (BVA) to solve both the feedthrough reliability problem and the issue of connecting control electronics to a high number of stimulating electrodes.

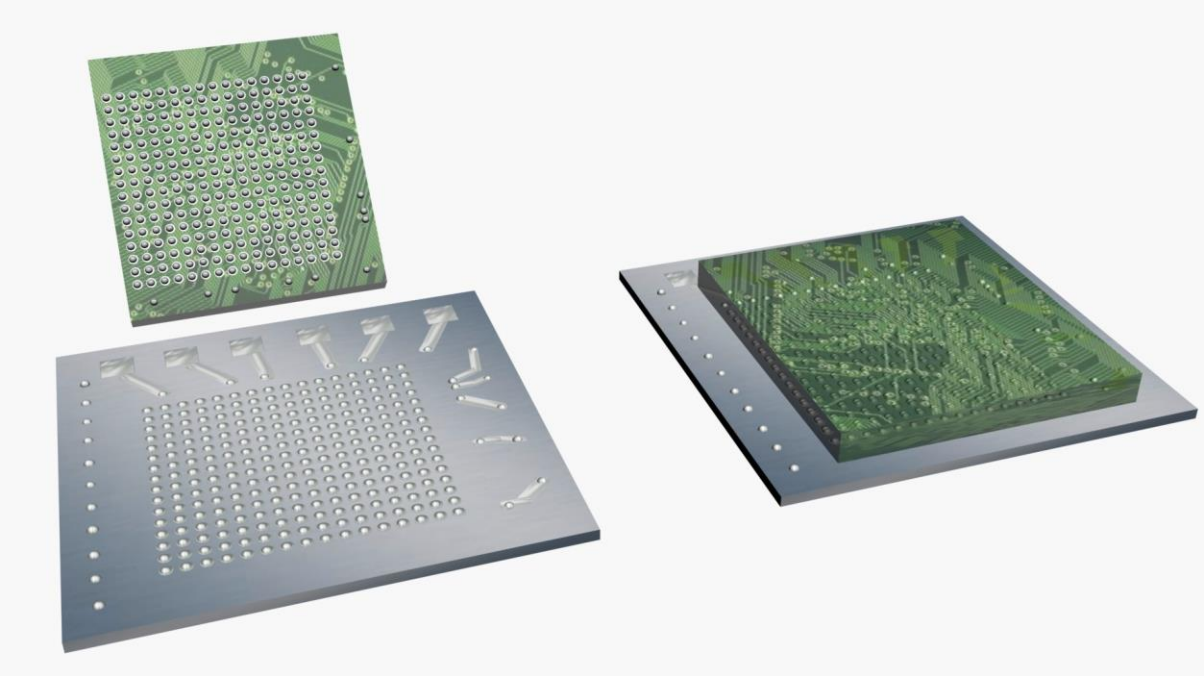

Figure 1. Illustration of the Bionic Vision Australia diamond feedthrough and electrode array (grey) with 256 hermetic feedthroughs leading to N-UNCD stimulating electrodes. The array measures 4 × 4 mm square and 0.25 mm in thickness. The diamond feedthrough array and stimulator chip are shown separately on the left and again after flip chip bonding of the two components on the right.

The illustration shows an array of diamond feedthroughs and electrodes. The feedthrough array (grey) is constructed from two types of diamond; a polycrystalline, electrically insulating diamond substrate containing many electrically conducting nitrogen doped ultra nano-crystalline diamond (N-UNCD) feedthroughs. On the flip side of the array (shown in Figure 2 (c)) the feedthroughs terminate in isolated N-UNCD pads which are employed as the stimulating electrodes of retinal prosthesis. We have previously shown that N-UNCD has

appropriate electrochemical characteristics to act as a neural stimulation material [9,10]. The fact that the substrate and feedthroughs are made from the same material, i.e. diamond, minimizes the possibility of feedthrough failure through materials mismatch, resulting in increased reliability. Importantly for our application the mechanical strength and low density of diamond means the capsule can be made thinner and lighter than it could be if made from a ceramic or a metal such as titanium. The approach also takes advantage of diamonds established biocompatibility [11-13] and superb biochemical stability [14] offering the prospect of a long lasting implant. Finally, the pitch and shape of the array shown in Figure 1 has been designed to be directly flip chip bonded to a purpose built ASIC capable of delivering electrical stimulation through 256 independently controllable channels. Direct bonding of the stimulator to the array negates the need for a high count lead to the electrodes and thus the technology is easily scalable to higher numbers of electrodes. The metal tracks on the inner side diamond array (Figure 1, right and upper edge) connect to a small number of supply power leads, forward data leads, counter electrode lead, backward data lead and power decoupling capacitors. Following is a description of the method employed to fabricate the diamond arrays and results of hermeticity, electrical testing and cytotoxicity testing.

2. *Materials and methods*

2.1 Feedthrough fabrication process

Thermal management grade polycrystalline diamond wafers (TM100 grade, 10 mm × 10 mm × 0.25 mm, element six Ltd) were used as the feedthrough substrates. The diamond wafers were supplied with one smooth face (<1 nm RMS roughness) and one very rough face. The rough face was polished to <10 nm RMS surface roughness using a resin bonded wheel on a Coborn PL3 rotary polisher (Figure 2 (a)). Feedthrough arrays were fabricated within the polished diamond wafers according to the schematic shown in Figure 2. 150 µm deep 80 µm square pits were milled into the polished PCD substrate in 150 µm pitch square arrays (Figure 2 (b)) with an Oxford Lasers Alpha series laser cutter fitted with a Nd:YAG laser operating at 532 nm. In a second step, 9 × 10 µm diameter feedthrough holes were cut into the bottom of each pit penetrating through the remaining 100 µm of substrate diamond (Figure 2 (c).

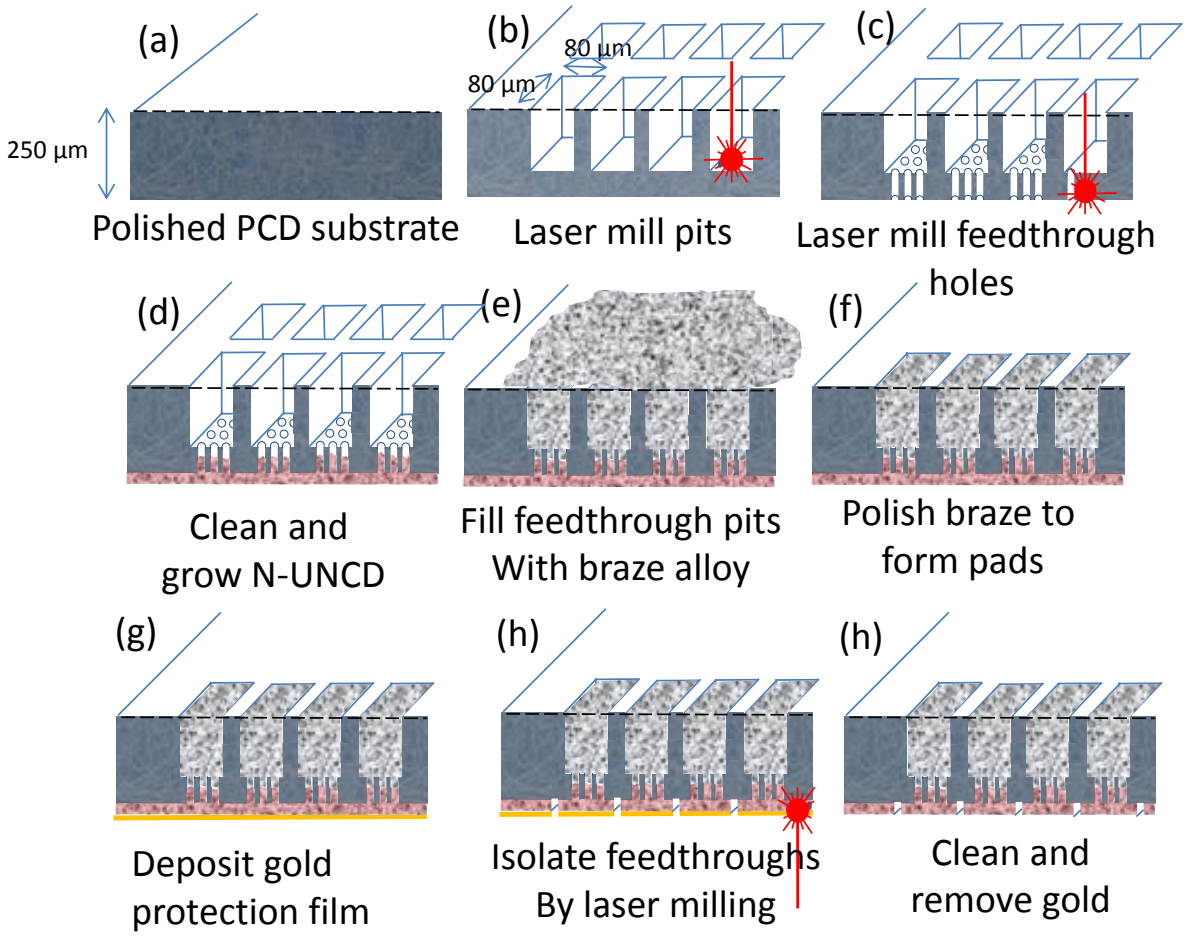

Figure 2. Process of fabricating diamond feedthrough array

After laser milling, graphitic cutting residues were removed from the substrate by boiling under reflux in a mixture of 10 mL H_2SO_4 (conc) containing 1g of $NaNO_3$ for 60 min followed by 30 min of 50 W 3:1 Ar:O_2 plasma (Diener FEMTO LF). N-UNCD was grown within the feedthrough holes and over the array face by microwave chemical vapour deposition (CVD) (iPlas, Cyrannus 1 Plasma source, Figure 2 (d)) using a gas mixture of 20% N_2, 79% Ar and 1% CH_4. CVD parameters were 1250 W microwave power, 100 Torr chamber pressure and a stage temperature of 800 ^{o}C. Full details of N-UNCD synthesis have been previously described [9]. A 100 nm thick, gold layer was deposited onto the N-UNCD surface with a Thermionics VE-180 e-beam Coating System (Figure 2 (e)) to protect the electrodes during subsequent plasma cleaning. Individual feedthroughs were isolated from one another by laser milling through the gold and N-UNCD films and slightly into the PCD substrate (Figure 2 (h) followed by 4-8 h of 50 W 3:1 Ar:O_2 plasma to remove the electrically conducting, graphitic, laser cutting residues from between N-UNCD electrodes. To make electrical contact with the inside of the feedthroughs the pits were filled with silver active

braze alloy (ABA). Silver-ABA (Wesgo metals, Morgan Technical Ceramics) was purchased in paste form and applied directly into the pits and over the back of the feedthrough arrays. The braze was melted into the feedthrough pits by heating the diamond substrate with an electron beam (Thermionics VE-180 Coating System, chamber pressure $< 1 \times 10^{-5}$ mbar, Figure 2 (g)). Once the braze melted, (approximately 930 ^{o}C) the arrays were held at temperature to allow the braze time to penetrate into the feedthrough holes. Finally, excess braze was removed from the array by mechanical polishing with a 1200 grit diamond impregnated steel wheel on a Coborn PL3 polisher (Figure 2 (h)) forming flat sliver contact pads on one side of the array. The gold protection layer was removed using a I_2:KI:H_2O 1:4:40 gold etch solution.

2.2 Imaging and focussed ion beam cross section

Scanning electron microscope imaging (SEM) was conducted either on a JEOL JSM 500 or a NOVA Nanolab SEM. The Nova Nanolab SEM also contained the focussed ion beam (FIB, gallium ions) used to obtain cross sectional images of feedthroughs. Optical imaging was performed on a Leica compound microscope.

2.3 Hermeticity testing

Hermeticity tests were conducted using an Adixen ASM310 Portable Helium Leak Detector on feedthrough arrays prepared without Silver-ABA back filling and without gold coating of the N-UNCD electrodes to show that the diamond forms the hermetic seal. Samples were mounted into a custom made holder such that an array of 60 feedthroughs was clamped between two Viton O-rings. One side of each sample was exposed to atmosphere and one side to the vacuum of the helium leak detector. Once baseline vacuum pressure was achieved, a slow flow of helium was introduced to the external face of the array. Samples with holes present permitted helium to pass through to the detector with a detection limit of 1×10^{-11} mbarLs^{-1}.

2.4 Electrical measurements

Electrical resistance of the feedthroughs and isolation tests were measured using a tungsten needle probe station connected to a Keithley 2400K voltage source and current meter. Isolation was measured by placing the 5 x 5 array electrode side down in a dry polystyrene Petri dish and placing the probe station probes on the Silver-ABA pads on the back of the

array. Isolation was measured using a potential of 6 V. Feedthrough resistance measurements were conducted by attaching the electrode array to a metal plate using silver paint (RS Components) and placing one probe on the metal plate and one on the Silver-ABA pad at the back of the feedthrough. Probe contact resistance and contribution of the silver paste were not accounted for but their effects were deemed to be minimal. To ensure that the favourable electrochemical properties of the N-UNCD stimulating electrodes were retained, cyclic voltammograms (CVs) were recorded on an eDAQ EA161 potentiostat controlled by an eDAQ ED410 data recorder connected to the pins of the probe station. The array was placed electrode side down in a polystyrene dish containing nylon cloth soaked in 0.9% sterile saline and held in place with a probe station pin pressed onto a Silver-ABA pad at the back of the feedthrough. A 2 mm diameter platinum pellet, pressed into the wet cloth served as a counter electrode and a 1 M Ag/AgCl reference electrode (CHI Instruments) was used. For electrical impedance measurements, constant current pulses were generated using an in-house built, optically isolated constant current stimulator. Electrodes were stimulated with cathodic-first, charge balanced biphasic pulses. The duration of each phase and the interphase gap were kept constant at 500 μs per phase and 25 μs, respectively. Voltage excursions were measured using a sensitive voltmeter (PXI-4072, National Instruments).

2.5 Growth of Neurons on N-UNCD

To ensure the biocompatibility of N-UNCD grown using our methods toward neurons, the viability of rat cortical neurons cultured N-UNCD was assessed. Cortical neurons were obtained by isolating the cerebral cortices from one-day-old rats, as previously described [15]. The meninges were removed and the cortical tissue dissociated by protease digestion for 20 min using 10 ug / mL Dnase 1 (Roche) and 250 ug / mL trypsin (Sigma) in HEPES buffered Eagles Medium (Gibco). Trypsinisation was terminated by using Soybean Trypsin Inhibitor (Sigma) / 10 ug / mL DNAse 1 and cells were pelleted by centrifuging, then titrated using a P1000 pipette. Finally, cells were diluted in culture medium consisting of Neurobasal A with 2% B27 supplement, 2mM Glutamax, 100U/ml penicillin and 100ug/ml streptomycin (all from Gibco) and seeded onto diamond samples at a concentration of 4×10^4 cellscm^{-2}. The cell cultures were then incubated at 37 ^{o}C in 5% CO_2. Cells were fixed after 24 hours with 4% paraformaldehyde for 20 min, permeabilized with methanol and then immunostained with rabbit anti-βIII tubulin (Promega) and the nuclear stain DAPI using standard protocols and imaged using fluorescent optical microscopy.

3.*Results*

3.1 Imaging

SEM images of the inside of a feedthrough pit and a single feedthrough hole are shown in Figure 3 (a) and (b). In this instance the Silver-ABA fill has been removed by dissolution in 2.5 M HNO_3 to show the structure of the diamond only. Figure 3 (c) shows the external face of a feedthrough array with flat 120 µm square pads of N-UNCD covering the feedthrough holes. Figure 3 (d) is a close up view of the N-UNCD surface showing the very high nano-scale roughness that occurs under our growth conditions.

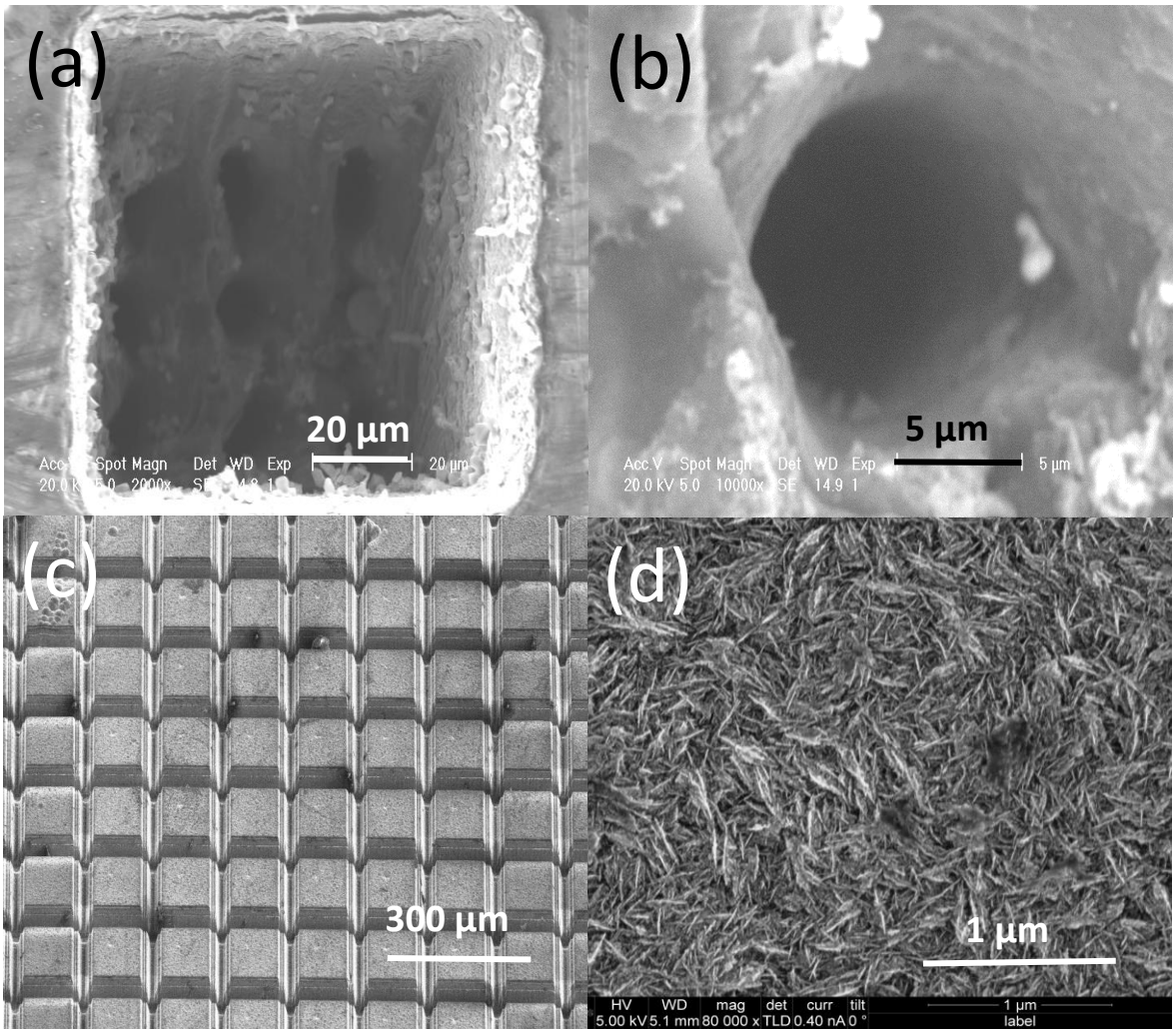

Figure 3. SEM images of (a) the inside of a feedthrough after removal of Silver-ABA fill. (b) Close up of a single feedthrough hole. (c) The structure of the external face of a feedthrough array after isolation of individual electrodes by laser. (d) Close up of the N-UNCD electrode surface shown in (c).

Figure 4 shows a cross sectional SEM image of a single feedthrough hole. For this image the external N-UNCD pad was polished away and a focussed ion beam has been employed to slice through the feedthrough, revealing both the horizontal and vertical N-UNCD / PCD interfaces. The N-UNCD inside the feedthrough hole has been coloured red because otherwise it is difficult to distinguish between the two materials. No voids or gaps are visible at the N-UNC / PCD interface.

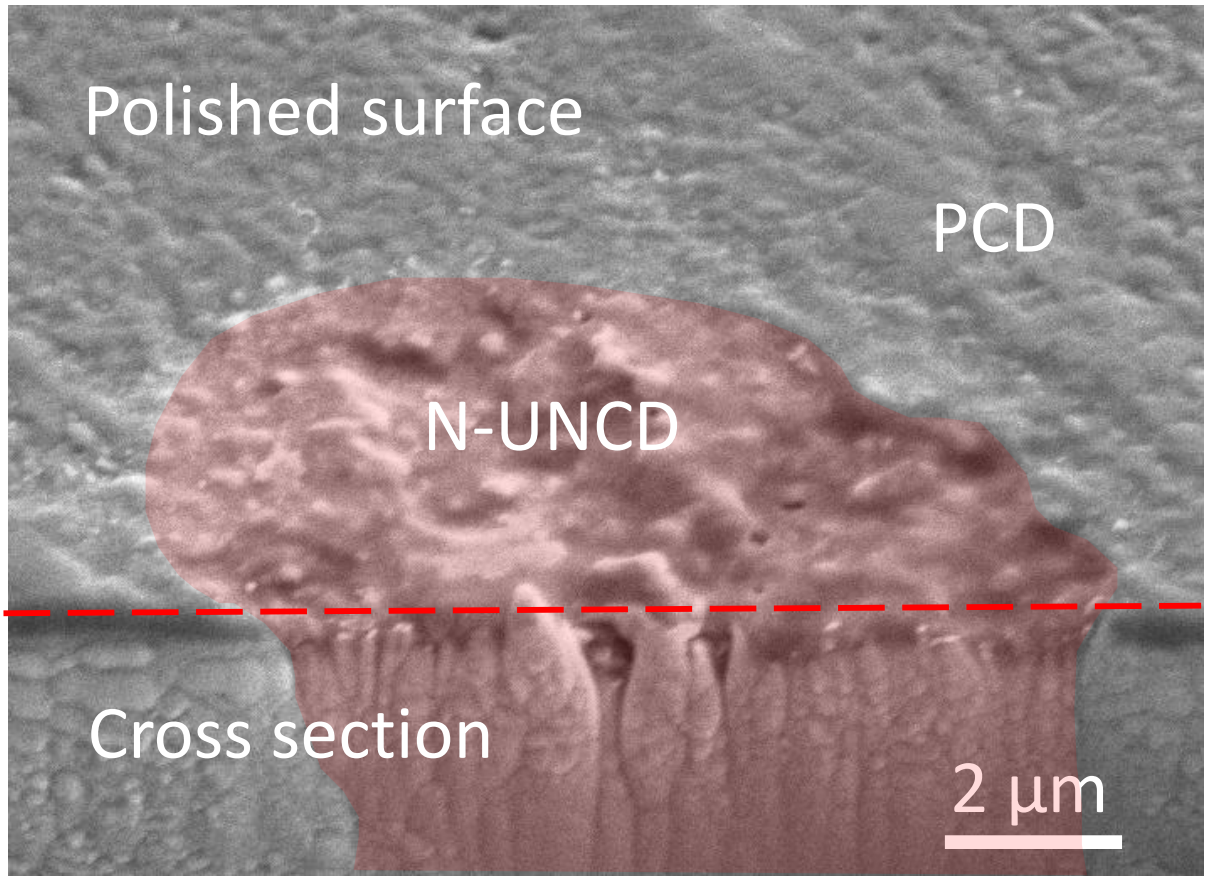

Figure 4. SEM image of a focussed ion beam cross section of a single N-UNCD filled feedthrough hole. The electrode surface has been polished back to expose just the feedthrough and the N-UNCD has been coloured to heighten contrast.

3.2 Hermeticity Testing

Figure 5 shows typical helium leak detection traces recorded from two hermetic, 60 way feedthrough samples (blue and red traces) one positive control sample (purple trace) and one negative control sample (green trace). The results illustrate the short test window (10-15 s)

available before helium saturates and leaks through the rubber o-rings between which the sample is secured. The traces recorded using the two hermetic arrays exhibit a similar profile

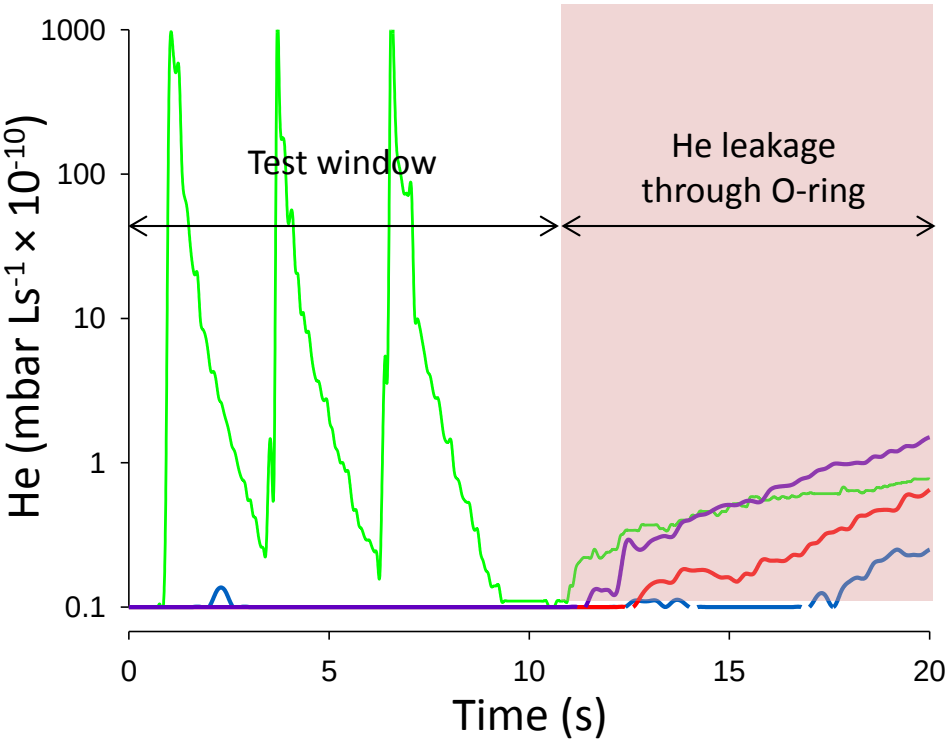

Figure 5. Helium leak test of three arrays with 60 feedthroughs in each array. One array contained a known leak (green trace) and two typical hermetic arrays are shown (red and blue traces). The purple trace is a positive control recorded from a fresh sheet of PCD with no feedthroughs.

to the positive control and no spike within the test window. Therefore the helium leak rate through the hermetic arrays is less than the detection limit of experiment (1×10^{-11} mbarLs^{-1}). All samples were subjected a constant slow flow of helium except for the negative control (green trace) which was subjected to three short bursts of helium to illustrate the rapid response observed when a leak is present in the sample.

3.3 Electrical testing

Table 1 shows the isolation resistance between all electrode pair combinations for a dry array and the resistance of each of the 25 feedthroughs from the same 5 × 5 array. The electrode layout is indicated on the table using the letters A-Y. The lowest isolation resistance measured was 3.3 MΩ between adjacent electrodes I and H. The average isolation between orthogonally adjacent electrodes was 250 MΩ with a standard deviation of 300 MΩ. The average isolation over all electrode pairs was 509 MΩ with a standard deviation of 368 MΩ.

A value of 1000 MΩ was noted for all measurements above the measurement limits of the equipment used. The average feedthrough resistance (Table 1 inset) was 43 Ω with a standard deviation of 14 Ω. Current-voltage (IV) curves for all feedthroughs were linear and exhibited slopes consistent with the measured resistance values. Figure 6 (a) shows the IV curves for the lowest (H), highest (U) and an average resistance (E) feedthrough.

Resistance between pairs of electrodes ($\Omega \times 10^6$)

	A	B	C	D	E	F	G	H	I	J	K	L	M	N	O	P	Q	R	S	T	U	V	W	X
Y	>1000	>1000	>1000	>1000	>1000	>1000	>1000	>1000	>1000	>1000	>1000	>1000	>1000	>1000	>1000	>1000	>1000	>1000	>1000	>1000	>1000	>1000	>1000	>1000
X	>1000	>1000	>1000	>1000	>1000	>1000	>1000	860	670	750	750	740	420	380	720	>1000	630	380	165	600	670	370	230	
W	>1000	>1000	>1000	>1000	>1000	>1000	>1000	890	880	920	820	760	690	660	930	>1000	16	580	550	830	425	71		
V	>1000	>1000	>1000	>1000	>1000	>1000	>1000	890	830	890	790	740	650	650	920	>1000	570	570	550	810	266			
U	>1000	>1000	>1000	>1000	>1000	800	800	650	670	720	600	570	510	530	770	410	390	470	490	700				
T	700	>1000	>1000	980	750	430	550	240	400	430	290	230	300	225	92	>1000	380	240	190					
S	232	520	620	600	440	147	172	65	100	167	114	70	54	17	220	>1000	157	48						
R	200	480	600	590	290	126	149	47	55	122	92	48	8.7	29	278	920	78							
Q	530	700	>1000	790	560	240	266	160	188	260	197	150	115	144	430	890								
P	>1000	>1000	>1000	>1000	>1000	>1000	>1000	>1000	>1000	>1000	>1000	>1000	100	>1000	>1000									
O	>1000	>1000	>1000	>1000	780	490	500	280	370	400	380	280	230	220										
N	190	296	590	590	400	112	135	44	78	136	82	41	11											
M	144	250	500	500	220	79	100	15	23	78	53	20												
L	100	220	460	450	235	55	82	46	55	117	26													
K	45	160	260	270	230	17	47	80	87	150														
J	270	550	700	640	480	165	176	37	30															
I	172	450	560	550	420	100	112	3.3																
H	154	280	560	260	490	94	100																	
G	36	145	230	220	280	11																		
F	11	100	170	180	230																			
E	190	150	69	53																				
D	135	87	9																					
C	120	72																						
B	60																							

Resistance of feedthroughs (Ω)

A	B	C	D	E		40	31	34	39	43
F	G	H	I	J		43	27	24	32	46
K	L	M	N	O		32	32	30	30	57
P	Q	R	S	T		65	41	29	36	55
U	V	W	X	Y		74	55	53	48	73

Table 1. Isolation and through resistance of 25 feedthroughs arranged as indicated on the table using the letter A-Y. Isolation resistances greater than 1 GΩ were recorded as 1000 MΩ. Feedthrough resistances are shown adjacent to and correspond with the electrode layout.

Figure 6 (b) shows a CV recorded in 0.9% sterile saline. The CV shows the wide electrochemical window typical of diamond. Onset of water oxidation in the anodic direction occurs at approximately 1.5 V, lower than some other forms of diamond [16] but consistent with our earlier work [9,10]. Water reduction onset occurs below -1.6 V yielding a usable water window of 3.1 V. Figure 6 (c) shows the voltage measured between a single isolated N-UNCD electrode and a large surface area platinum return electrode in response to stimulation with a single 50 µA amplitude constant current pulse. Two results showing the upper and lower limits of the dataset are shown. Polarisation of the electrode surface is represented by the sloping part of the voltage excursion as indicated on the plots by a red dotted line. The capacitance of the electrode is calculated from the slope of this line using the formula $C = I/(dV/dt)$ where C = capacitance (F), I = pulse amplitude (A) and (dV/dt) is the slope of the polarisation part of the voltage excursion. Using a conservative safe water window of -1 to

1V this capacitance value translates directly to a charge injection limit range for the electrodes of 23- 27 nC. The

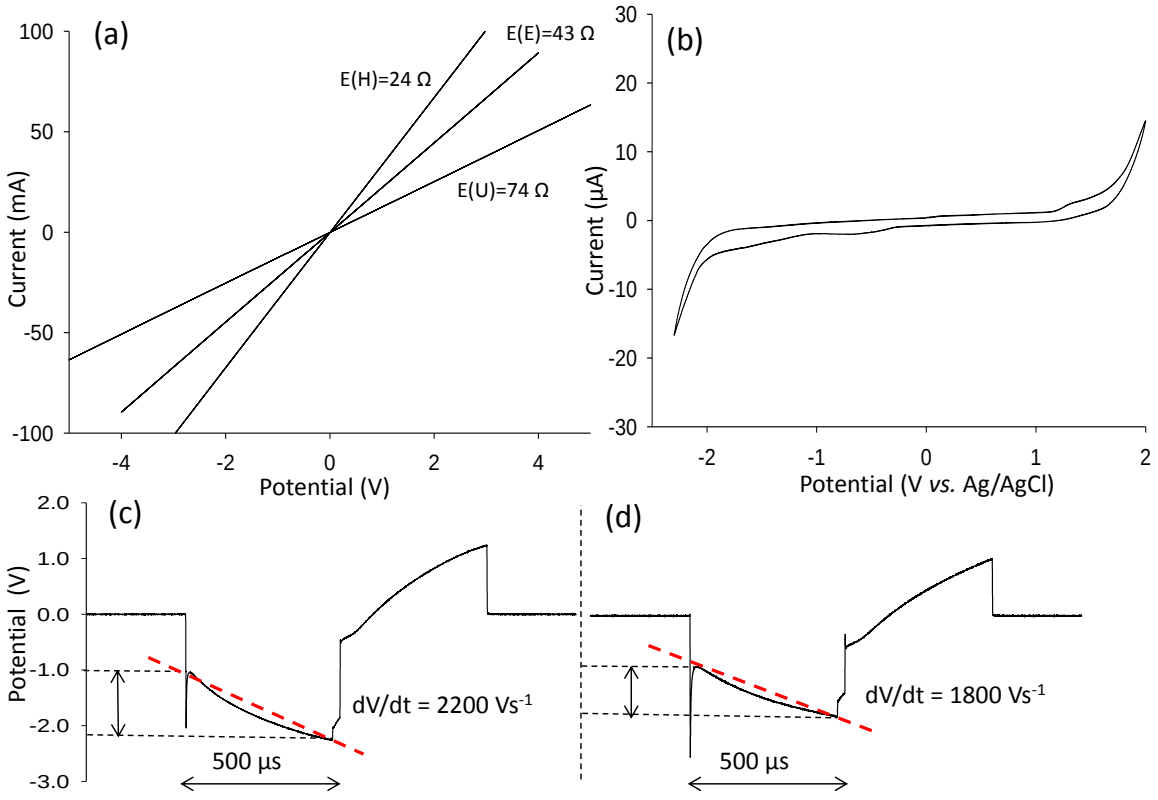

Figure 6. (a) IV curves recorded through the lowest (H) highest (U) and an average resistance (E) feedthrough. (b) CV recorded in 0.9 % sterile saline, scan rate 0.1 Vs^{-1}. Voltage excursions recorded during 500 µs per phase cathodic first biphasic constant current pulses for a high (c) and a low (d) impedance electrode. The voltage excursions (dV/dt) from which capacitance values are derived are indicated on the plots

charge injection capacity for N-UNCD is derived from this value by dividing the charge injection limit by the geometric electrode area of 1.44×10^{-4} cm^2 (120 × 120 µm) yielding a range of 158 - 193 μCcm^{-2}.

3.4 Growth of Neurons on N-UNCD

Figure 7 (a) is a histogram showing the average neuron counts per mm^2 for rat cortical neurons grown on N-UNCD, PCD and tissue culture plastic (TCP) for 24 h. Neurons survived in high numbers on both N-UNCD and PCD with lower survival on TCP indicating that neither forms of diamond is inherently cytotoxic. Higher densities of healthy neurons

were observed on N-UNCD than PCD. Figure 7 (b) is a confocal microscope image of stained neurons grown on N-UNCD. The neurons appear healthy and many exhibit neurite outgrowth.

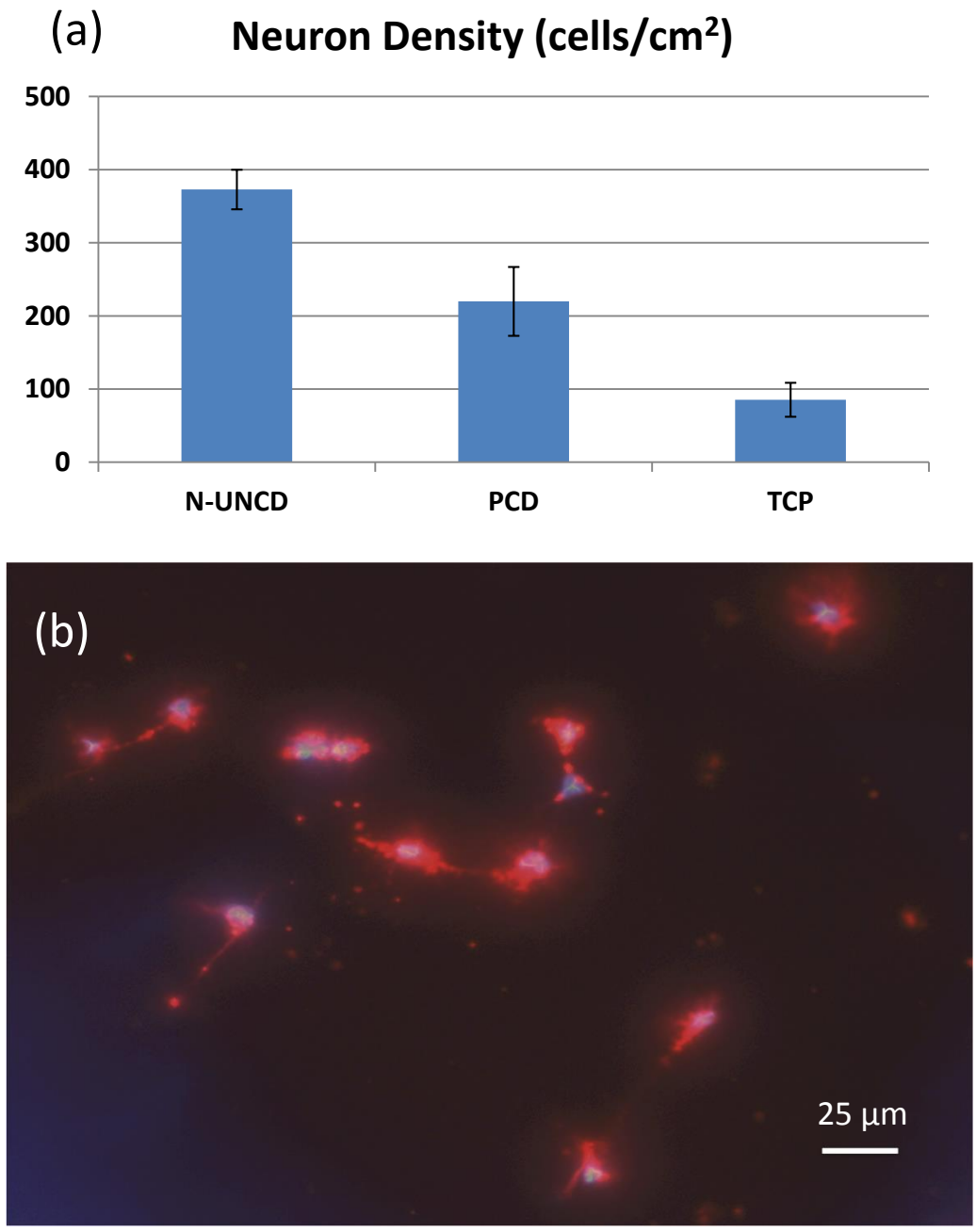

Figure 7. (a) Counts of surviving rat cortical neurons grown on N-UNCD, PCD and TCP after 24 h of incubation. (b) Confocal microscope image of rat cortical neurons on N-UNCD exhibiting neurite outgrowth.

4. Discussion

It is important to note that many of the dimensions listed for fabrication of the feedthrough array described in this paper have been chosen to fit a specific application. The provided dimensions are by no means a prescriptive set of parameters for a hermetic feedthrough array. An example is the substrate thickness of 250 µm which was chosen for reasons of mechanical strength and to allow latitude for shaping of the array face to fit the curvature of the eye. The 150 µm deep pits are a consequence of choosing such a thick substrate. The first reason for the pits is that it is not possible to mill very thin holes through 250 µm of diamond using our laser so the pits are a method of thinning the diamond substrate. Thin feedthrough holes are required to reliably form hermetic feedthroughs. Secondly, it is clear from Figure 3 (b) that N-UNCD grown on the far side of array does not penetrate all the way through the 100 µm length of the feedthrough hole. Though an untested theory, we postulated that Silver-ABA braze was unlikely to be able to penetrate through a very long narrow feedthrough hole and contact the N-UNCD reliably. The pits serve the purpose of bringing the braze closer to the N-UNCD buried in the feedthrough holes. During lead up work hermetic feedthroughs were successfully generated in 100 µm thick free standing PCD sheets provided by Delaware Diamond Knives. Thin Silver-ABA contact pads (10-20 µm deep) were employed in this instance to provide reliable bonding pads to electronic components but pits to thin the substrate were not required. Free standing PCD films as thin as 30 or 40 µm have been used in other work and can be handled though films of this these thicknesses are very delicate. The choice of nine feedthrough holes per pit is also a parameter that could be readily varied. The choice of nine holes in our work was made in order to minimise the resistance of each feedthrough within the constraints of our device design. The maximum feedthrough hole density is obviously a function of the thickness of the substrate and the quality of the system used to drill the holes. The 25 µm pitch for the feedthrough holes depicted in Figure 3 (a) is a lower limit for a hole length of 100 µm using our laser system without holes beginning to merge with one another.

One parameter that is relatively more rigid is the diameter of the feedthrough holes themselves. Figure 3 (b) shows the widest point of a single feedthrough hole at 10 µm. The view shown in Figure 3 (b) is the same side as that from which the hole is cut and, due to the conical shape of the focussed laser, the hole tapers to around 3-5 µm on the N-UNCD growth side of the feedthrough. Workers experienced in laser milling will appreciate that a high quality laser system with high resolution optics and precision stage are required to generate structures with such small dimensions. The feedthrough holes in this example were cut using

the full 2.7 W of laser power available, pulsed at 5 kHz, focussed 50 µm into the substrate and held for several seconds. At lower power with thinner substrates smaller holes are likely to be achievable though the feedthroughs will exhibit a corresponding increase in resistivity. In our system, growth rates of N-UNCD in the CVD chamber do not exceed 1 µm/h. Filling feedthrough holes much bigger than 5 µm in diameter with low failure rates for hermeticity becomes extremely time expensive at these growth rates. Therefore possessing a high resolution method of forming small feedthrough holes, with precision, is a requirement of the fabrication method. Though all of the steps involved in fabricating these arrays can be conducted at wafer level, laser milling and N-UNCD growth are still slow processes so the fabrication method is most compatible with high value product such as a neural prosthesis.

The importance of removal of graphitic residue after laser milling cannot be overstated. We found that if substrates were not cleaned N-UNCD failed to grow reliably within the feedthrough holes resulting in leaks. It is well established that a diamond seed or diamond surface is required in order to successfully grow more diamond by CVD. We conclude that the Ar:N_2 gas mixture and plasma conditions used to grow N-UNCD are insufficient to remove graphitic residue from the substrate and that the graphitic laser damage is an unsuitable surface for diamond growth. Before growth of N-UNCD a harsh wet etch could be used to remove graphite because no sensitive materials or components have been added to the array at this point. After N-UNCD growth and isolation of the feedthroughs by laser milling only O_2 plasma was used to gently remove residues between electrodes. Figure 2 (h) shows the point in the fabrication process when laser isolation occurs. At this point Silver-ABA is present and the thin gold protection film on the N-UNCD, both of which would be damaged during an acid boil step. The gold film is added to protect the N-UNCD electrodes during handling but most importantly to protect the electrodes during the long O_2 plasma treatment required to remove graphite from between electrodes. We estimated in our previous work [9] that N-UNCD films grown with 20% N_2 in the reaction chamber could have as much as 50% sp^2 bonding, (or graphitic character) in the matrix [9]. The term UNCD was popularised by Argonne laboratories where such films were most heavily researched. The term generally refers to films of very small diamonds (3-5 nm) held together by amorphous carbon grain boundaries. Rather than acting as a traditional dopant, the introduction of N_2 when growing N-UNCD films appears to widen the grain boundaries and give them a more graphitic character [17,18]. This phenomenon is thought to explain the high conductivity of N-UNCD films compared with UNCD films grown without N_2. As our N-UNCD electrodes are used

for neural stimulation it is vital that the favourable electrochemical properties [9,10] (e.g. high electrochemical capacitance) be protected. Hydrogen and nitrogen plasmas have been shown to reduced sp^2 content in N-UNCD films, changing the electrical performance [19]. It follows that oxygen plasma is likely to similarly etch away sp^2 bonded carbon in the grain boundaries of the N-UNCD electrodes and change the electrochemical performance therefore a protection film is a prudent step.

Figure 4 shows the conformality with which the N-UNCD grows within the PCD feedthrough holes. Without the red colouration it is difficult to distinguish the boundary between the two materials attesting to an intimate contact. The adhesion between the UNCD film and the PCD substrate is exceptionally strong even after nitrogen inclusion. Delamination between N-UNCD has not been observed by us during this work or previously. Provided that the array has been given sufficient N-UNCD growth time for the feedthrough holes to close over, arrays are reliably hermetic. An advantage of the fabrication system is that arrays that exhibit a leak during testing can be returned to the CVD chamber for an additional layer of N-UNCD until all feedthrough holes are closed. Electrically insulating UNCD has been shown by other workers to able to function as a hermetic coating *in vitro* and *in vivo* when grown directly on a silicon substrate [14,20]. In that work the authors showed that hermetic films of UNCD could be grown at temperatures as low as 400 ^{o}C [14]. Though this is a remarkably low temperature for UNCD growth it is still well above the maximum temperature specification of 250 ^{o}C for the BVA microstimulator chip. In our work the substrate temperature during optimised growth of N-UNCD feedthroughs exceeds 1000 ^{o}C. Thus our diamond encapsulation must be constructed as a stand-alone capsule within which the chip is sequestered once all CVD steps are completed.

Isolation of the feedthroughs by laser milling through the N-UNCD film is a straight forward process but does require removal of electrically conducting graphitic laser milling residues from between the electrodes. Because the array contains metal components at this time point acid etching is not an option thus oxygen plasma was used. We found that extended periods (approximately 30 h) were required to achieve reasonable isolation between electrodes using a 50 W plasma asher with a 10% O_2 in Argon gas mixture. Undoubtedly this time could be reduced significantly if a higher power reactive ion etcher were used. Providing that the Silver-ABA contacts on in the feedthrough pits has been polished sufficiently remaining graphitic residues are the primary source of shorting between electrodes. The lower average

isolation resistance 250 MΩ for adjacent electrodes compared to 509 MΩ between all electrode pairs is strong evidence of this. Higher power graphite etching conditions will likely also improve isolation. For our purposes where the feedthroughs are driving small stimulating electrodes where the electrode solution impedance is likely to be 20 – 40 kΩ, MΩ isolation resistances are acceptable if the feedthroughs were being used to drive a higher impedance process then better isolation could be required. Likewise the electrode / solution impedance values of 20-40 kΩ renders the feedthrough resistance of 20 -70 Ω acceptable. If a lower feedthrough resistance was required then the feedthrough pitch may need to be increased so that more N-UNCD channels could be used per feedthrough. The variability in the feedthrough resistance encountered in the work described here appears to rise from errors during cutting of the feedthrough holes at the bottom of the pits. The feedthrough hole pitch is close to the operational limits of the laser used and small errors in alignment result in less than nine feedthough holes penetrating through to the external face for a single feedthrough. We assume that low resistance feedthroughs contain nine feedthrough holes and high resistance feedthroughs some number less than nine. This variability is a process control issue and is the subject of ongoing work.

Figure 6 (a) shows a linear IV curves for three different feedthroughs and are representative of the data set. The slopes of all the IV curves agreed with measured resistances within 2% variation in all cases. All curves were linear with no changes in slope that would indicate interface barriers or rectification of current. It is notable that the braze interface with N-UNCD is also included in this measurement. Silver-ABA brazes adhere to diamond by virtue of a 1.25 % loading of titanium in the mixture which forms a Ti-C layer at the braze / diamond boundary during heating [21,22]. It appears that this contact is ohmic and therefore suitable for inclusion in the feedthrough. Thermally annealed carbide formers such as Ti or Mo are often used to form ohmic contacts to conducting forms of diamond [23]. N-UNCD has been shown to form ohmic contacts with a number of metals even without thermal annealing [24] therefore an ohmic contact between the family of Ti-C forming brazes and N-UNCD is likely. The CV shown in Figure 6 (b) is consistent with N-UNCD and does not show any detectable metal contamination that may have occurred during fabrication. The charge injection capacity range of 153 - 198 μCcm^{-2} established in section 3.3 is similar to that established in our previous work of 169 μCcm^{-2} [9]. 169 μCcm^{-2} is considered a reasonable value for a neural stimulation material. For instance the most popular neural

stimulation material, platinum, has published charge injection values between 50 and 150 μCcm^{-2} [25].

Biocompatibility is naturally a primary concern when fabricating a medical implant. PCD [12,26], UNCD [11,13,20] and N-UNCD [27,28] have all been extensively studied and invariably prove to be highly biostable and non-cytotoxic. We conducted a cytotoxicity assay on our N-UNCD using rat cortical neurons to ensure there were no peculiarities in our system. The results in section 3.4 show that N-UNCD grown using our conditions is non-cyctotoxic, consistent with the previous reports. An exciting prospect with N-UNCD is that previous reports indicate that UNCD and N-UNCD are not only non-cytotoxic but may promote healthy neural integrations with the surface [27-29]. Figure 7 (a) shows that neurons survived with higher densities on N-UNCD than PCD and on both materials survival was significantly higher than on the TCP control. Higher survival rates of neurons on UNCD over TCP controls has been previously demonstrated [30]. In that work Voss *et al.* observed healthy functioning of insect circadian pacemaker neurons on UNCD by measuring intracellular Ca^{+} concentration fluctuations. Figure 7 (b) also shows that healthy neurite growth is able to occur on our N-UNCD. This is further evidence that N-UNCD may promote healthy nerve interactions and may actively facilitate effective electrical stimulation.

5. Conclusion

A versatile scalable method has been developed to fabricate dense hermetic micro arrays of electrical feedthroughs consisting of conducting N-UNCD channels within an insulating PCD substrate. The arrays exhibited sufficiently low feedthrough resistance and sufficiently high isolation resistance to function as a retinal stimulation array. Electrochemical testing of the N-UNCD electrodes terminating the feedthroughs showed that the favourable electrochemical properties of the N-UNCD were not lost during the fabrication process and that all electrical contacts within the feedthroughs were ohmic in character. Finally, a cytotoxicity assay showed survival of rat cortical neurons and neurite outgrowth on N-UNCD indicating that the material is non-cytotoxic and a suitable tissue interface for a biomedical implant.

6. Acknowledgements

NICTA is funded by the Australian Government as represented by the Department of Broadband, Communications and the Digital Economy and the Australian Research Council

through the ICT Centre of Excellence program. The Bionics Institute acknowledges the support they receive from the Victorian Government through its Operational Infrastructure Program. This research was supported by the Australian Research Council (ARC) through its Special Research Initiative (SRI) in Bionic Vision Science and Technology grant to Bionic Vision Australia (BVA).

7. References

[1] Jiang GQ, Zhou DD In *Implantable Neural Prostheses 2: Techniques and Engineering Approaches*; Zhou, D. D., Greenbaum, E., Eds. 2010, p 27-61.
[2] Ong JM, da Cruz L. The bionic eye: a review. Clin Experiment Ophthalmol. 2012;40:6-17.
[3] Guenther T, Lovell NH, Suaning GJ. Bionic vision: system architectures - a review. Expert Rev Med Devic. 2012;9:33-48.
[4] Zrenner E, Bartz-Schmidt KU, Benav H, Besch D, Bruckmann A, Gabel VP Et al. Subretinal electronic chips allow blind patients to read letters and combine them to words. Proc R Soc B. 2011;278:1489-97.
[5] Zrenner E. Artificial Vision Solar cells for the blind. Nature Photonics. 2012;6:342-43.
[6] Yanai D, Weiland JD, Mahadevappa M, Greenberg RJ, Fine I, Humayun MS. Visual performance using a retinal prosthesis in three subjects with retinitis pigmentosa. Am J Opthalmol. 2007;143:820-27.
[7] SecondSight. Arguss II System Overview. http://2-sight.eu/en/system-overview-en.
[8] Bron AJ, Wolff E, Tripathi RC, Tripathi BJ *Eugene Wolff's anatomy of the eye and orbit*; Capman and Hall Medical, 1997.
[9] Garrett DJ, Ganesan K, Stacey A, Fox K, Meffin H, Prawer S. Ultra-nanocrystalline diamond electrodes: optimization towards neural stimulation applications. J Neural Eng. 2011;9:016002.
[10] Hadjinicolaou AE, Leung RT, Garrett DJ, Ganesan K, Fox K, Nayagam DAX Et al. Electrical stimulation of retinal ganglion cells with diamond and the development of an all diamond retinal prosthesis. Biomaterials. 2012;33:5812-20.
[11] Amaral M, Dias AG, Gomes PS, Lopes MA, Silva RF, Santos JD Et al. Nanocrystalline diamond: In vitro biocompatibility assessment by MG63 and human bone marrow cells cultures. J Biomed Mater Res. 2008;87A:91-99.
[12] Aspenberg P, Anttila A, Konttinen YT, Lappalainen R, Goodman SB, Nordsletten L Et al. Benign response to particles of diamond and SiC: Bone chamber studies of new joint replacement coating materials in rabbits. Biomaterials. 1996;17:807-12.
[13] Bajaj P, Akin D, Gupta A, Sherman D, Shi B, Auciello O Et al. Ultrananocrystalline diamond film as an optimal cell interface for biomedical applications. Biomed Microdevices. 2007;9:787-94.
[14] Auciello O, Shi B In *Implantable Neural Prostheses 2: Techniques and Engineering Approaches*; Zhou, D. D., Greenbaum, E., Eds. 2010, p 63-84.
[15] Goldshmit Y, Greenhalgh CJ, Turnley AM. Suppressor of cytokine signalling-2 and epidermal growth factor regulate neurite outgrowth of cortical neurons. Eur J Neurosci. 2004;20:2260-66.
[16] Waldvogel SR, Elsler B. Electrochemical synthesis on boron-doped diamond. Electrochim Acta. 2012;82:434-43.
[17] Birrell J, Carlisle JA, Auciello O, Gruen DM, Gibson JM. Morphology and electronic structure in nitrogen-doped ultrananocrystalline diamond. Appl Phys Lett. 2002;81:2235-37.
[18] Birrell J, Gerbi JE, Auciello O, Gibson JM, Gruen DM, Carlisle JA. Bonding structure in nitrogen doped ultrananocrystalline diamond. J Appl Phys. 2003;93:5606-12.

[19] Jeedigunta S, Xu ZQ, Hirai M, Spagnol P, Kumar A. Effects of plasma treatments on the nitrogen incorporated nanocrystalline diamond films. Diamond Relat Mater. 2008;17:1994-97.
[20] Xiao XC, Wang J, Liu C, Carlisle JA, Mech B, Greenberg R Et al. In vitro and in vivo evaluation of ultrananocrystalline diamond for coating of implantable retinal microchips. J Biomed Mater Res B. 2006;77B:273-81.
[21] Hsieh YC, Lin ST. Interfacial Bonding Strength Between Brazing Alloys and CVD Diamond. J Mater Eng Perform. 2009;18:312-18.
[22] Buhl S, Leinenbach C, Spolenak R, Wegener K. Influence of the brazing parameters on microstructure, residual stresses and shear strength of diamond-metal joints. J Mater Sci. 2010;45:4358-68.
[23] Moazed KL, Zeidler JR, Taylor MJ. A thermally activated solid-state reaction process for fabricating ohmic contacts to semiconducting diamond. J Appl Phys. 1990;68:2246-54.
[24] Gerbi JE, Auciello O, Birrell J, Gruen DM, Alphenaar BW, Carlisle JA. Electrical contacts to ultrananocrystalline diamond. Appl Phys Lett. 2003;83:2001-03.
[25] Cogan SF. Neural stimulation and recording electrodes. Annu Rev Biomed Eng. 2008;10:275-309.
[26] Tang L, Tsai C, Gerberich WW, Kruckeberg L, Kania DR. Biocompatibility of Chemical-Vapor-Deposited Diamond. Biomaterials. 1995;16:483-88.
[27] Thalhammer A, Edgington RJ, Cingolani LA, Schoepfer R, Jackman RB. The use of nanodiamond monolayer coatings to promote the formation of functional neuronal networks. Biomaterials. 2010;31:2097-104.
[28] Specht CG, Williams OA, Jackman RB, Schoepfer R. Ordered growth of neurons on diamond. Biomaterials. 2004;25:4073-78.
[29] Chen YC, Lee DC, Hsiao CY, Chung YF, Chen HC, Thomas JP Et al. The effect of ultra-nanocrystalline diamond films on the proliferation and differentiation of neural stem cells. Biomaterials. 2009;30:3428-35.
[30] Voss A, Wei H, Muller C, Popov C, Kulisch W, Ceccone G Et al. Influence of the surface termination of ultrananocrystalline diamond/amorphous carbon composite films on their interaction with neurons. Diamond Relat Mater. 2012;26:60-65.